Signature of Hanle precession in trilayer MoS_{2}: Theory and experiment

K. Tian, Z. Yue, D. Magginetti, M. E. Raikh, and A. Tiwari

Phys. Rev. B **95**, 174428 — Published 18 May 2017

DOI: 10.1103/PhysRevB.95.174428

Signature of Hanle Precession in Trilayer MoS_2: Theory and Experiment

K. Tian[1], Z. Yue[2], D. Magginetti[1], M. E. Raikh[2], and A. Tiwari[1]
[1]*Department of Materials Science and Engineering, University of Utah, Salt Lake City, UT 84112, USA*
[2]*Department of Physics and Astronomy, University of Utah, Salt Lake City, Utah 84112, USA*

Valley-spin coupling in transition-metal dichalcogenides (TMDs) can result in unusual spin transport behaviors under an external magnetic field. Nonlocal resistance measured from 2D materials such as TMDs via electrical Hanle experiments are predicted to exhibit nontrivial features, compared with results from conventional materials due to the presence of intervalley scattering as well as a strong internal spin-orbit field. Here, for the first time, we report the all-electrical injection and non-local detection of spin polarized carriers in trilayer MoS_2 films. We calculate the Hanle curves theoretically when the separation between spin injector and detector is much larger than spin diffusion length, λ_s. The experimentally observed curve matches the theoretically-predicted Hanle shape under the regime of slow intervalley scattering. The estimated spin life-time was found to be around 110 *ps* at 30 K.

PACS numbers: 72.25.Dc, 75.40.Gb, 73.50.-h, 85.75.-d

I. INTRODUCTION

The discovery of two-dimensional (2D) transition metal dichalcogenides (TMDs) has attracted considerable attention recently due to their exotic properties, which are very important for their applications in electronic, optoelectronic, and spintronic devices [1–4]. The members of the TMD family possess spin as well as valley degrees of freedom which make them attractive for next-generation quantum computing applications too. One of the most studied examples of above materials is MoS_2, which, contrary to graphene, possesses a band gap of $\Delta = 1.9$ eV in its monolayer form [5–7]. The valleys in 2D MoS_2 are located at two energetically equivalent symmetry points, K and K', in the hexagonal Brillouin zone. Because of large spin orbit coupling (SOC) which originates from the d orbitals of heavy Mo atoms [8–14], and the inversion asymmetry induced Dresselhaus coupling [15–19], the valence band edges of 2D MoS_2 undergo a large spin splitting ($\lambda \sim$150 meV). In the case of conduction band, there is a competition between the contributions from the d orbitals of the Mo atoms and the p orbitals of the S atoms which results in much smaller spin-orbit splitting in the conduction band than that in the valence band. Furthermore, the Hamiltonian of 2D MoS_2 possesses time reversal symmetry, which leads the two valleys to exhibit opposite sign of spin-orbit field, see Fig.1 [16,20–22]. Because of the above unique characteristics, both the spin as well as valley degrees of freedom can be addressed and manipulated in 2D MoS_2, leading to its potential for applications in next-generation valleytronics-based devices.

Despite MoS_2's great potential in future spintronic devices, there are still very few experimental studies on the spin transport and relaxation mechanisms operating in the material [23–27]. Among those, the most noteworthy study is by Yang *et al.* [26] in which they used optical Hanle-Kerr experiment to measure the spin-valley dynamics in 2D MoS_2 and observed a long spin lifetime of 3 *ns* at 5 K. Though the above observation is very important for obtaining fundamental understanding of the spin-valley dynamics, it is also important to explore spin transport characteristics of the material using all-electrical techniques. Nonlocal Hanle techniques have been widely used to investigate spin transport in several semiconducting systems, see e.g. Refs. [28–35], however, there are no such reports for 2D MoS_2.

In nonlocal Hanle measurements, spin polarized carriers are injected into the semiconductor channel from a magnetized ferromagnetic electrode. Accumulated spin-polarization just below the injector electrode diffuses in the channel and creates spin imbalance below the detector electrode which is again made of a ferromagnetic metal. This imbalence in spin results in a voltage signal in the detector. However, when a transverse magnetic field is applied, the spin of the electrons starts precessing around the applied field with Larmor frequency [36–38]. Because of the combined effect of spin precession and spin dephasing, the spin accumulation and hence the voltage signal at the detector decays with magnetic field following the shape known as Hanle curve. The shape of the Hanle curve yields important information about spin lifetime and spin diffusion length.

One reason which is probably responsible for the lack of reports on nonlocal Hanle studies on 2D MoS_2 is that large area films were not availabe until recently. Nonlocal Hanle experiments require four electrode contacts and at least two of those contacts must be long enough so that their shape anisotropy preserve their in-plane magnetization when a traverse magnetic field is applied. These experimental requirements are indeed quite challenging in the case of micron sized MoS_2 films normally produced by exfoliation based techniques. However, recently the growth of centimeter-scale high-quality 2D MoS_2 films by CVD and PVD techniques has been demonstrated by several groups [3,39,40]. Availability of these relatively large area films now can catalyze the spin transport studies on this exotic material system.

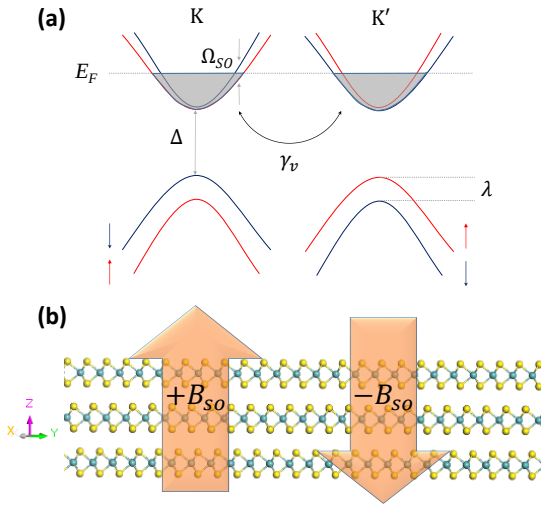

FIG. 1: (a) Schematic of energy spectrum of trilayer MoS_2 at K and K' valleys. Ω_{SO} is the spin splitting at the Fermi level; λ is the spin splitting at valence band top; and Δ is the band gap. Intervalley scattering rate, γ_v, is determined by short range impurities. (b) Bottom scheme indicates the internal spin orbital field, $\pm B_{SO}$, induced by spin orbital coupling along z direction in the case of trilayer MoS_2. Here we find it appropriate to mention that there is still no consensus about whether $K(K')$ or Q point of the Brillouin zone should be the minima of the conduction band for trilayer MoS_2. Recent report by Brumme et al [22]showed that for relatively high electron doping ($1.69 \times 10^{14}\ cm^{-2}$), all 8 minima in the conduction band may be populated. However, they showed that for relatively lower doping level ($2.25 \times 10^{13}\ cm^{-2}$), only the minima at $K(K')$ point are occupied. Based on our Hall effect results which showed that the carrier concentration in our films was $1.3 \times 10^{13}\ cm^{-2}$ at 30 K, we assumed that the later (i. e. electrons populating only the minima at K and K''s points) is the case.

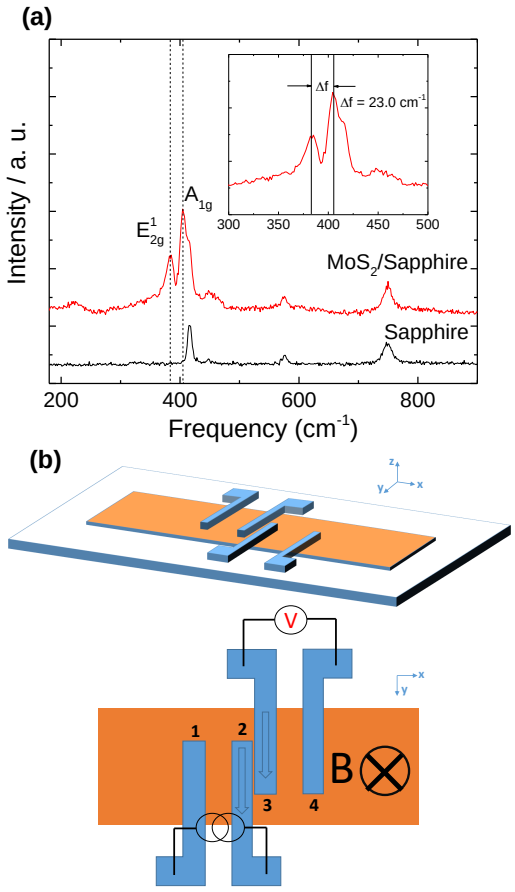

FIG. 2: (a) Raman spectra of trilayer MoS_2. The separation of vibration frequency E^1_{2g} and A_{1g} indicates three monolayers of MoS_2. (b) Schematic illustration of Hanle experiments performed through electrical methods on trilayer MoS_2, three dimensional view and top view. The measure of a nonlocal resistance is a voltage between right two contacts (3 and 4), while the current flows through the first two contacts (1 and 2), which are made of 15 nm NiFe. The distance of middle two contacts (2 and 3), d (distance between the spin injector and detector) is 1 μm. We studied the Hanle curves under condition of $d > \lambda_s$. The arrows in the FM indicate the magnetization direction and also the spin polarization direction. Hanle experiments were performed under normally oriented external magnetic field.

Other important factor, which possibly precluded the Hanle studies is the fact that electrically injected spin-polarized electrons in 2D MoS_2 experience a very strong out-of-plane intrinsic magnetic field due to the spin-orbit splitting in the conduction band. In our previous theoretical study, we showed that the Hanle curve under normal field orientation is expected to exhibit a two-peak structure with maxima located at the values of external field $B = \pm B_{SO}$, where B_{SO} is internal spin-orbit field. For monolayer MoS_2 the value of B_{SO} is in the range of a few Tesla [41]. Thus, in experiments where the measurements are performed over a small out-of-plane external field interval, the peaks cannot be detected.

While the strength of SOC in monolayer MoS_2 is expected to be the strongest, it is expected that SOC will also be present in other inversion asymmetric odd-layered MoS_2 films, see Ref. [17]. The magnitude of SOC is supposed to decrease on increasing the number of layers. As a result, the two peaks will get progressively closer and might fall within the measurement range.

With this motivation, we performed nonlocal Hanle measurements on trilayer MoS_2 films and obtained non-trivial results, which we report in this paper. To compare these results with theory, we have also extended our previous theoretical work Ref. [42] to incorporate the case of a finite distance between injector and detector.

The paper is organized as follows. In Section II, we discuss the sample preparation, characterization and Hanle experiments. Section III describes a theoretical model used in our study. In Section IV, we present our experimental Hanle results and compare them with theory.

II. EXPERIMENTAL DETAILS

Trilayer MoS_2 films were grown on sapphire substrates by pulsed laser deposition (PLD) following the procedure described in previous report [39]. The number of monolayers deposited was controlled precisely by controlling the number of laser pulses. After deposition, Raman spectra were collected from the MoS_2 films as shown in Fig. 2(a). The two Raman vibrational modes, E^1_{2g} and A_{1g}, confirm the presence of MoS_2. In prior studies it has been demonstrated that the separation between these modes can be used to determine the number of monolayers [3]. The observed peak separation of 23.0 cm^{-1} in the present study confirmed the formation of trilayer MoS_2 [39,43].

Electrical Hanle measurements were conducted using a four probe geometry as shown in Fig. 2(b). The pattern of ferromagnetic (FM) contacts was fabricated through photolithography, and electron beam evaporation was used to deposit 15 nm thick NiFe contacts. After lift-off, the edge-to-edge separation of the middle two contacts was found to be 1 μm. Hall effect measurements were performed to determine the carrier concentration in the as-grown films.

I-V measurements performed between contact 1 and 2 showed the presence of a Schottky barrier between NiFe and MoS_2. Presence of this barrier elinimated the need for depositing any additional tunnel barrier layer[44,45]. To determine the Schottky barrier height (Φ_B), temperature dependent I-V curves were recorded. Fig.3(a) shows the I-V curves at different temperatures on a logarithmic scale. The barrier height was extracted using the thermionic emission function described in Appendix A. For this, first of all, $In(I_{12}/T^{3/2})$ vs. $1000/T$ was plotted for various V_{12} values as shown in Fig. 3(b). In the next step, slopes of these plots were determined as a function of V_{12} (see Fig. 3(c)). From the y-axis intercept of Slope vs. V_{12} plot, value of Schottky barrier height was determined to be 41.3 mV. For Hanle measurement, the current was passed between first two contacts, 1 and 2, while the non-local voltage, V_{34}, is measured through the other two contacts, 3 and 4.

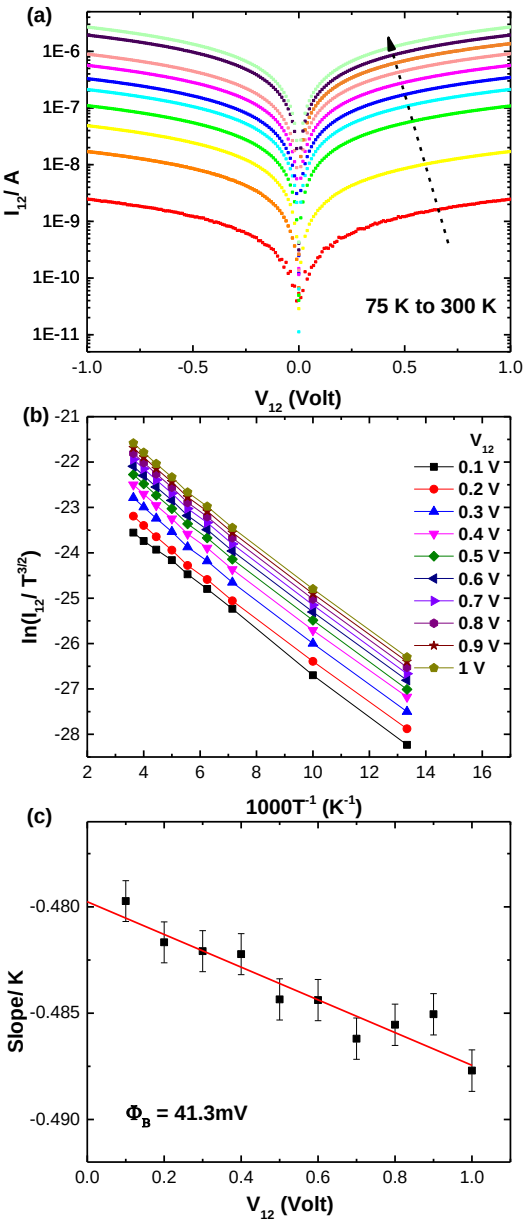

FIG. 3: (a) I-V curves of the trilayer MoS_2 sample with NiFe contacts from 75 K to 300 K. (b) Arrhenius plots, In $(I_{12}/T^{3/2})$ vs 1000 T^{-1}, at different V_{12}. (c) Extraction of Schottky barrier height,Φ_B.

III. THEORY

In the theory of the Hanle effect [36,37,46–48], the nonlocal resistance, $R(\omega^z_L)$, is related to the spin density, $S_x(t)$, as follows

$$R(\omega^z_L) = \frac{P^2 D\rho}{A}\int_0^\infty dt S_x(t) P_d(t), \qquad (1)$$

where ω^z_L is the Larmor frequency, $\omega^z_L = \mu_B g B/\hbar$, μ_B is the Bohr magneton, g is the g-factor, B is the magnetic field, $\hbar$ is the reduced Planck constant, P is the spin injection/detection polarization, D is the diffusion coefficient related to the mobility (μ) via the Einstein relation, $D = \mu k_B T/e$, ρ is the resistivity of channel material, A is the cross-sectional area of the channel, and $P_d(t)$ is the diffusion propagator defined as:

$$P_d(t) = \frac{1}{(4\pi Dt)^{1/2}} \exp\Big(-\frac{d^2}{4Dt}\Big) \qquad (2)$$

In above equation, d denotes the distance between the injector and detector electrodes.

The shape of the Hanle curve depends on the relation between d and the spin diffusion length, λ_s. In Ref. [42] we considered the case $d \ll \lambda_s$. With regard to our present experimental study, the opposite limit $d \gg \lambda_s$ is relevant. Physically, in this limit, the Hanle curve is expected to exhibit numerous oscillations due to the fact that the spin of injected electron can accomplish integer number of full precessions before it reaches the detector [47].

The unique characteristics of the spin dynamics in TMDs originates from the fact that there exist two groups of spins corresponding to two valleys K and K'. Due to a finite intervalley scattering rate, γ_v, the time evolution of $\boldsymbol{S}^K(t)$ and $\boldsymbol{S}^{K'}(t)$ is described by the following system of coupled equations:

$$\frac{d\boldsymbol{S}^K}{dt} = (\Omega_{SO}+\omega_L^z)\hat{z}\times\boldsymbol{S}^K - \gamma_v\left(\boldsymbol{S}^K-\boldsymbol{S}^{K'}\right),$$
$$\frac{d\boldsymbol{S}^{K'}}{dt} = -(\Omega_{SO}-\omega_L^z)\hat{z}\times\boldsymbol{S}^{K'} + \gamma_v\left(\boldsymbol{S}^K-\boldsymbol{S}^{K'}\right), \quad (3)$$

where $\Omega_{SO} = \mu_B g B_{SO}/\hbar$. The above equations reflect the fact that the external field, ω_L^z, adds to the internal spin-orbit field Ω_{SO} in the valley K and $-\Omega_{SO}$ in the valley K', see Fig. 1. As is shown from the above relation, the value of spin splitting at the Fermi energy depends directly on the value of g. In principle the value of g can be calculated by using the methodology described in the paper by Li *et al* [49]. However, this requires the knowledge of the exact positions of the band edges in trilayer MoS_2. Since, at this time we do not know these positions, we assumed a value of 2 for g. This assumption is based on the reports by Kormányos *et al* [12] and Yang *et al* [26] in which they showed a g value of 1.8 for monolayer MoS_2. For trilayer, which is closer to bulk, the difference of $g-2$ is expected to be even smaller.

The system Eq. (3) should be solved with initial conditions, $\boldsymbol{S}(0) = \hat{x}$, which reflects the fact that at the moment of injection the spin is directed along the x-axis. In our earlier paper Ref. [42] we have demonstrated that the analytical solution of the system depends on the dimensionless ratio

$$\Gamma = \frac{\gamma_v}{\Omega_{SO}}. \quad (4)$$

For a slow intervalley scattering, $\Gamma < 1$, the solution for the x projection of the net spin, $S_x(t) = S_x^K(t) + S_x^{K'}(t)$, reads

$$S_x(t) = \frac{1}{2}\left\{\frac{\Gamma}{\sqrt{1-\Gamma^2}}\left[\sin\left(\omega_L^z+\tilde{\Omega}_{SO}\right)t - \sin\left(\omega_L^z-\tilde{\Omega}_{SO}\right)t\right] + \left[\cos\left(\omega_L^z+\tilde{\Omega}_{SO}\right)t + \cos\left(\omega_L^z-\tilde{\Omega}_{SO}\right)t\right]\right\}\exp\left[-\Gamma\Omega_{SO}t\right], \quad (5)$$

where we have introduced modified spin-orbit coupling

$$\tilde{\Omega}_{SO} = \sqrt{1-\Gamma^2}\Omega_{SO}. \quad (6)$$

From Eq. (5) the calculation of nonlocal resistance is straightforward and the result can be obtained in a closed form. This is apparent, because, in the absence of spin-orbit coupling, the integral of the product $\exp(i\omega_L^z t)P_d(t)$ appears in the expression for the conventional Hanle shape and can be evaluated analytically. In our case, $S_x(t)$ is the combination of two oscillating functions. Final result for $R(\omega_L^z)$ reads

$$R(\omega_L^z) = R_0\Bigg\{\left(\frac{\pi}{|y_+|}\right)^{1/2}\exp\left[-2|y_+|^{1/2}\cos\phi_+\right]\cos\left(\phi_+ + 2|y_+|^{1/2}\sin\phi_+\right)$$
$$+\left(\frac{\pi}{|y_-|}\right)^{1/2}\exp\left[-2|y_-|^{1/2}\cos\phi_-\right]\cos\left(\phi_- + 2|y_-|^{1/2}\sin\phi_-\right)$$
$$-\frac{\Gamma}{\sqrt{1-\Gamma^2}}\Bigg\{\left(\frac{\pi}{|y_+|}\right)^{1/2}\exp\left[-2|y_+|^{1/2}\cos\phi_+\right]\sin\left(\phi_+ + 2|y_+|^{1/2}\sin\phi_+\right)$$
$$-\left(\frac{\pi}{|y_-|}\right)^{1/2}\exp\left[-2|y_-|^{1/2}\cos\phi_-\right]\sin\left(\phi_- + 2|y_-|^{1/2}\sin\phi_-\right)\Bigg\}\Bigg\}. \quad (7)$$

R_0 is the prefactor which depends on spin injection/detection polarization, channel dimensions, and material resistivity [50]. Parameters $y_\pm$ and $\phi_\pm$ entering into Eq. (7) are defined as:

$$|y_\pm| = \tilde{d}^2\left[1+\left(\omega_L^z \pm \tilde{\Omega}_{SO}\right)^2(\tau_s^*)^2\right]^{1/2},$$
$$\phi_\pm = \frac{1}{2}\arctan\left[\left(\omega_L^z \pm \tilde{\Omega}_{SO}\right)\tau_s^*\right], \quad (8)$$

where $\tilde{d}$ is the dimensionless distance

$$\tilde{d} = \frac{d}{\lambda_s} = \frac{d}{(D\tau_s^*)^{1/2}}, \tag{9}$$

and τ_s^* is the inverse spin relaxation rate. In the absence of other relaxation mechanisms, this rate is determined by the intervalley scattering rate. In the presence of additional mechanisms, this rate is the sum of the partial rates

$$\frac{1}{\tau_s^*} = \Gamma\Omega_{SO} + \frac{1}{\tau_s}. \tag{10}$$

A. The case of slow intervalley scattering

In Fig. 4 the Hanle curves plotted using Eq. (7) for two different values of spin-orbit field and several sets of τ_s^* are shown. For these plots, the value of parameter Γ was chosen to be $\Gamma = 0.2$. As can be seen, the nonlocal resistance decays away from $B = \pm B_{SO}$ in an oscillatory fashion. Naturally, for shorter τ_s^*, the decay of oscillations is faster. For "strong" $B_{SO} = 1$ T (as in a monolayer) the most pronounced oscillations take place away from the origin. However, with regard to experiment, we are interested in the behavior of nonlocal resistance only within the domain $|B| < 0.2$ T. For this reason, the central regions of the plots are enlarged, as shown in the inset figures of Fig. 4 (a-c). We see that the evolution of the Hanle shape near $B = 0$ is quite lively, so that the shape changes significantly even when τ_s^* changes slightly from $\tau_s^* = 5$ ps and $\tau_s^* = 8$ ps. Still, the distance between the two maxima exceeds 0.2 T for all τ_s^* near $B = 0$. For a smaller value of the spin-orbit field, $B_{SO} = 0.1$ T, the behavior of nonlocal resistance near $B = 0$ evolves with increasing τ_s^* as follows. There are pronounced oscillations at $\tau_s^* = 20$ ps, less pronounced at $\tau_s^* = 100$ ps, and almost no oscillations for $\tau_s^* = 200$ ps, as shown in Fig. 4 (d-f). This behavior is the consequence of the fact that the bigger is τ_s^*, the more "bound" are the oscillations to the points $B = \pm 0.1$ T. Still, in all three curves the distance between the left and right extrema is close to 0.1 T near $B = 0$.

B. The case of fast intervalley scattering

For fast intervalley scattering we have $\Gamma > 1$ and the expression Eq. (7) for spin dynamics does not apply anymore. Physically, in the domain of fast intervalley scattering spin-orbit field effectively averages out as a result of fast switching of a carrier between the valleys. The modes of spin dynamics in the domain $\Gamma > 1$ are classified into valley-symmetric (we denote it with +) and valley-asymmetric (−). As a result of averaging out of $\pm B_{SO}$ the − mode has a long lifetime, $\sim \Omega_{SO}^2/\gamma_v$, while the lifetime of the symmetric mode is $\sim \gamma_v$. The actual

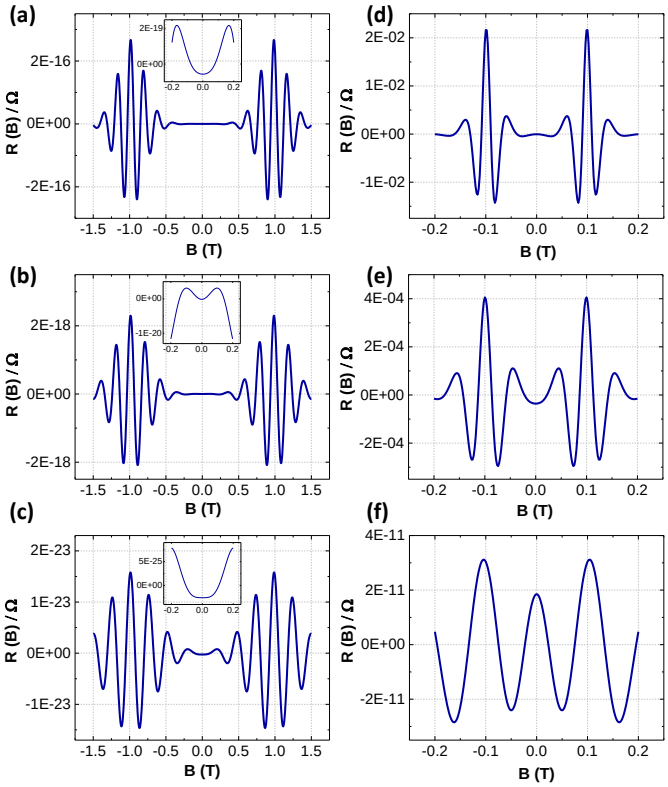

FIG. 4: Theoretical Hanle curve calculated from Eq. (7) in the case of slow intervalley scattering. In all six panels the value of parameter Γ is 0.2, the distance d is chosen to be $d = 1$ μm, and the diffusion coefficient is equal to $D = 2.6$ cm^2/s; (a) $B_{SO} = 1$ T, $\tau_s^* = 10$ ps, $\tilde{d} = 19.7$; (b) $B_{SO} = 1$ T, $\tau_s^* = 8$ ps, $\tilde{d} = 22.0$; (c) $B_{SO} = 1$ T, $\tau_s^* = 5$ ps, $\tilde{d} = 27.8$; (d) $B_{SO} = 0.1$ T, $\tau_s^* = 200$ ps, $\tilde{d} = 4.4$; (e) $B_{SO} = 0.1$ T, $\tau_s^* = 100$ ps, $\tilde{d} = 6.2$; (f) $B_{SO} = 0.1$ T, $\tau_s^* = 20$ ps, $\tilde{d} = 13.9$. Inset figures of (a-c) exhibit the zoom-in curve in smaller field range, $|B| < 0.2$ T.

form of $S_x(t)$ in the domain $\Gamma > 1$ is still the sum of the products of oscillating and exponentially decaying functions, as we have demonstrated in Ref. [42]. This allows to calculate the Hanle curve explicitly for finite separation, d, between the contacts. The result, representing the sum of contributions from + and − modes, reads

$$R(\omega_L^z) = R_0\Bigg\{\Big(1-\frac{\Gamma}{\sqrt{1-\Gamma^2}}\Big)\Big(\frac{\pi}{|Y_+|}\Big)^{1/2}\exp\Big[-2|Y_+|^{1/2}\cos\Phi_+\Big]\cos\Big(\Phi_+ + 2|Y_+|^{1/2}\sin\Phi_+\Big)$$
$$+\Big(1+\frac{\Gamma}{\sqrt{1-\Gamma^2}}\Big)\Big(\frac{\pi}{|Y_-|}\Big)^{1/2}\exp\Big[-2|Y_-|^{1/2}\cos\Phi_-\Big]\cos\Big(\Phi_- + 2|Y_-|^{1/2}\sin\Phi_-\Big)\Bigg\}. \quad (11)$$

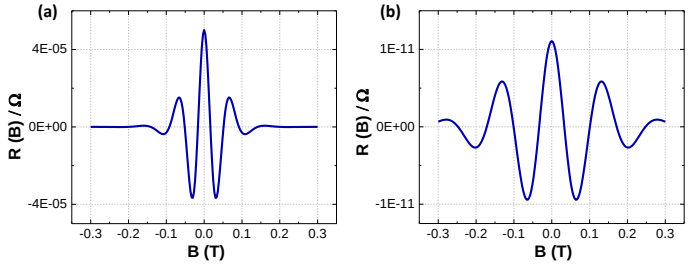

FIG. 5: Theoretical Hanle curve calculated from Eq. (11), $R(B)$ vs external field B, under conditions of $\Gamma = 2$ for different B_{SO} and $\tau^*_{s\pm}$. (a) $B_{SO} = 0.1$ T, $\tau^*_{s+} = 3$ ps, $\tau^*_{s-} = 68$ ps, $\tilde{d}_+ = 17.1$, $\tilde{d}_- = 7.5$; (b) $B_{SO} = 1$ T, $\tau^*_{s+} = 1.5$ ps, $\tau^*_{s-} = 18$ ps, $\tilde{d}_+ = 50.8$, $\tilde{d}_- = 14.9$.

The notations in Eq. (11) are the following

$$|Y_\pm| = \tilde{d}^2_\pm\Big[1+(\omega_L^z)^2(\tau^*_{s\pm})^2\Big]^{1/2},$$
$$\Phi_\pm = \frac{1}{2}\arctan\Big[\omega_L^z\tau^*_{s\pm}\Big]. \quad (12)$$

The relaxation times in Eq. (12) are defined as

$$\frac{1}{\tau^*_{s\pm}} = (\Gamma \pm \sqrt{\Gamma^2-1})\Omega_{SO} + \frac{1}{\tau_s}. \quad (13)$$

Two values of τ^*_s result in two spin diffusion lengths, $\lambda_{s\pm}$, so that $\tilde{d}_+$ in Eq. (12) is equal to d/λ_{s+} and $\tilde{d}_-$ is equal to d/λ_{s-}.

Fig. 5 shows the resulting Hanle curves calculated from Eq. (11) for different values of B_{SO}. A distinctive feature of these curves compared to Fig. 4 is that $R(B)$ falls off from $B = 0$ with oscillations, so that the maximum at $B = 0$ is the highest.

IV. EXPERIMENTAL HANLE DATA

Fig. 6 shows the experimental Hanle data recorded at 30 K (Data recorded at other temperatures are shown in Appendix B). Measurements of nonlocal resistance were performed using the experimental geometry shown in Fig. 2(b). Before measurements, injector and detector contacts were magnetized parallel to each other by applying an in-plane magnetic field which was parallel to the length of the electrode. Once the electrodes were

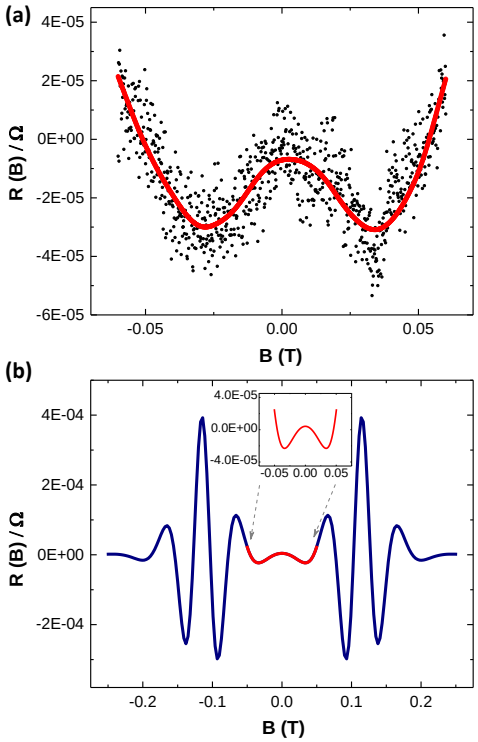

FIG. 6: (a) Experimental results, $R(B)$, in normal field (maximum 0.06 T) performed at 30 K. The red curve is the guide to eye line. (b) Calculated $R(B)$ curve using Eg. (7) in which the zoom-in portion of the curve matches the experimental result shown in (a).

magnetized, in-plane field was removed and a perpendicular magnetic field was applied to record Hanle data. To avoid the misalignment of the injector and detector magnetization, the out-of plane magnetic field was restricted between ±60 mT. For Hanle measurements, current was applied between electrode 1 and 2, and the voltage was measured between 3 and 4 while the transverse magnetic field was scanned from +60 mT to −60 mT.

Some salient features of the observed R_{NL} vs. B curve at 30 K are: (a) value of R_{NL} at $B = 0$ T is almost zero; (b) on increasing the magnetic field, the sign of R_{NL} becomes negative and its magnitude starts increasing on either side of $B = 0$ T; (c) at around $B = 0.03$ T, the magnitude of R_{NL} starts decreasing and finally at $B = 0.05$ T, again becomes zero; (d) after 0.05 T, R_{NL} be-

come positive and its magnitude increases with increase in field. The above features are obviously very different from the typical Hanle curves shown by normal materials where a maxima is observed at $B = 0$ T in R_{NL} vs. B curve. In order to understand the mechanism responsible for the observed behavior, we compared the experimental data with our theoretical prediction discussed in section III.

First of all, a quick comparison of the curve shown in Fig. 6(a) with theoretical curves shown in Fig. 4 and Fig. 5, suggested that the sample under investigation is in the regime $\Gamma < 1$. Specifically if the sample was in the regime $\Gamma > 1$, it should have exhibited a maxima at $B = 0$ T in R_{NL} vs. B curve. Once we found out the regime to which our sample belongs, we fitted the experimental data to the corresponding expression, i.e. equation (7). In Eq. (7), there are four independent unknown parameters namely, B_{SO}, τ_s^*, Γ, and μ, which were varied during the fitting procedure. Figure of merit of the fit was determined by calculating the quantity $\chi^2 = \frac{1}{N}\sum_{n=1}^{N}[\frac{Y_{data}-Y_{fit}}{Y_{error}}]^2$.

The experimental data was found to fit very well in Eq. (7) with a value of $\chi^2 = 1.16$. Fitted curve is shown by solid red curve in Fig. 6(a). The best fitting parameters were found to be $B_{SO} = 0.12 \pm 0.01$ T, $\tau_s^* = 110 \pm 10$ ps, $\Gamma = 0.35 \pm 0.05$, and $\mu = 900 \pm 50$ cm^2/Vs.

It is important to note that even though, because of experimental constraints, range over which we could scan the out-of-plane field was limited to ± 60 mT, we could estimate B_{SO} which was much higher than that field. Now using the experimentally determined values of B_{SO}, τ_s^*, Γ, and μ, in equation (7), we calculated the $R(B)$ curve over a magnetic field range of ± 0.25 T and obtained a curve shown in Fig. 6(b).

The curve exhibits two peak structure with maxima located at ± 0.12 T corresponding to two valleys. Furthermore, both of the peaks are accompanied with oscillatory signal on both sides of the main peaks which is understood to arise because of the integer number of full precession accomplished by the spin of the injected electrons before it reaches the detector electrode.

It is interesting to note that though the main Hanle peaks belonging to two valleys are well separated corresponding oscillatory peaks overlap near the origin and give rise to the shape in R_{NL} vs. B plot as observed in our experiment. See the part of curve shown in red line in Fig. 6(b).

To check the consistency of the fit, from the values of Γ and B_{SO} obtained above by the fitting of experimental data, we calculate the intervalley scattering rate $\gamma_v = \Gamma\Omega_{SO} = 7.4 \times 10^9$ s^{-1}. If the mobility is limited entirely by the intervalley scattering, it is related to γ_v and the carrier density n as [42]:

$$\mu = \left(\frac{\Delta}{\lambda}\right)\frac{e}{2\pi\hbar\Gamma n} = \left(\frac{\Delta}{\lambda}\right)\frac{e\Omega_{SO}}{2\pi\hbar\gamma_v n}. \qquad (14)$$

Using the value of mobility obtained from the fit, and the value of density $n = 1.3 \times 10^{13}$ cm^{-2} as determined from Hall effect data we got the value $\Gamma = 0.20$ in reasonable agreement with $\Gamma = 0.35$ inferred from the fit.

V. CONCLUDING REMARKS

(i) In summary, using the all-electrical technique of injecting and detecting spin polarized carriers, we have observed the signature of Hanle precession in trilayer MoS_2 films.
(ii) Our theoretical calculations showed that because of the valley-specific spin-orbit field present in the odd-layered MoS_2 films, two distinct Hanle peaks centered at $B = \pm B_{SO}$ are expected.
(iii) In the case of trilayer MoS_2, the strength of SO field is smaller than that for monolayer films. As a result, under certain experimental conditions, secondary oscillatory signals belonging to the two valleys can overlap and give rise to a detectable signal near the zero external magnetic field.
(iv) By comparing the experimental data with the theoretically predicted results, we found that the trilayer MoS_2 films prepared by PLD undergo a slow intervalley scattering which is very important from the point of view of realizing practical valleytronic devices. A spin life-time of around 110 ps was estimated at 30 K.
(v) In our theoretical model, we made following assumptions. Firstly, we assumed that, similar to monolayer, the minima of conduction band in trilayer MoS_2 is located at K and K' points. Secondly, we assumed that the interlayer scattering processes do not affect the spin relaxation in the trilayer MoS_2 so the model developed for the monolayer in Ref.[42] is also applicable to trilayers.
(vi) Here we find it interesting to bring into the reader's attention that in certain system, nontrivial spin transport effect can also arise because of the intervalley scattering and g-factor anisotropy as described by Li *et al* in Phys. Rev. Lett. **111**, 257204 (2013) [51].
(vii) Availability of large-area trilayer MoS_2 films, in which valley specific spin transport can be investigated by electrical means, is likely to expedite further research in this area.

VI. ACKNOWLEDGMENTS

This work was supported by NSF through grants No. 1407650 and 1121252.

Appendix A: Calculation of Schottky barrier height using thermionic equation

In the case of 2D materials, the thermionic emission equation is [45]:

$$I_{12} = A_{2D} S T^{3/2} \exp\Big[-\frac{q}{k_B T}\Big(\Phi_B - \frac{V_{12}}{n}\Big)\Big], \qquad \text{(A1)}$$

where A_{2D} is the 2D equivalent Richardson constant, S is the contact area between MoS_2 film and probe, q is electron charge, n is the ideality factor, k_B is the Boltzmann constant. The slope of the Arrhenius plot, $In(I_{12}/T^{3/2})$ vs 1000/T, is given by the expression:

$$S = -\frac{q}{1000 k_B}\Big(\Phi_B - \frac{V_{12}}{n}\Big). \qquad \text{(A2)}$$

Appendix B: Experimental Hanle Data at different temperatures

In order to gain further understanding, temperature dependent measurements were also performed over the temperature range between 10 K to 300 K. At temperatures below 30 K, because of the large resistance of the sample, which exceeded the compliance of our measurement system, the noise level was very high. On the other hand, for temperatures above 50 K, the strength of the Hanle signal was very weak and undetectable by our measurement system. So the useful temperature range of our study was 30 K - 50 K. Fig.7(a), (b), (c), (e), (g), and (i) show the plots of non-local resistance measured at 25 K - 55 K. As can be seen from Fig.7(a) and (b), we were not able to fit the Hanle results at 25 K and 55 K. However, at intermediate temperatures, the results resemble distinguishable shapes, which differ substantially as temperature varies.

We performed the fitting of these curves to the theory using Eq. (7) and concluded that the changes of the shape is due to shorter spin life time, smaller mobility, and stronger intervalley scattering rate as temperature increases. Table I presents the fitting parameters of Hanle results at various temperatures. Using these values, we calculated the $R(B)$ curve over a larger magnetic field range of ± 0.25 T and obtained the complete curve including the two major peaks, which is shown in Fig.7(d), (f), (h), and (j).

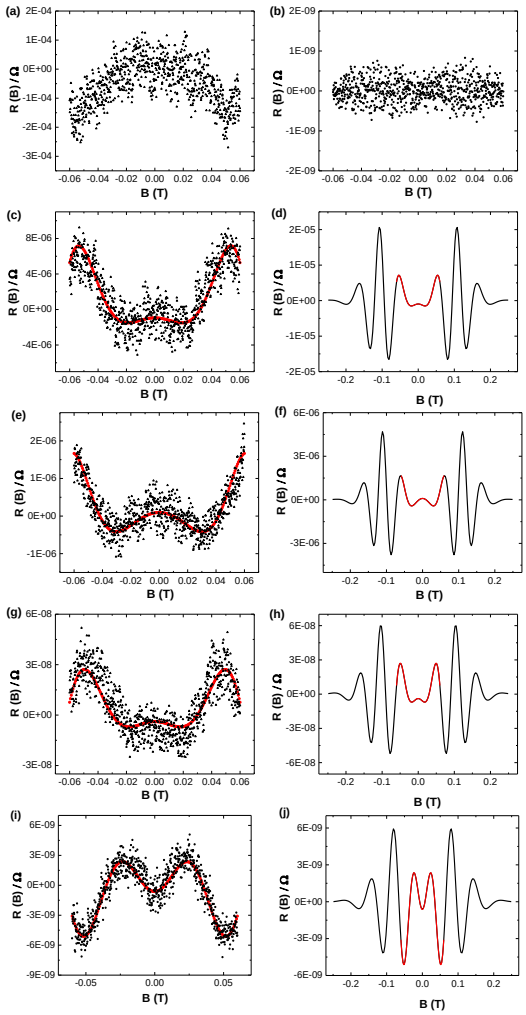

FIG. 7: Experimental Hanle data at (a) 25 K, (b) 55 K, (c) 35 K, (e) 40 K, (g) 45 K, and (i) 50 K. The calculated Hanle curves are also shown at various temperatures of (d) 35 K, (f) 40 K, (h) 45 K, and (j) 50 K, over the magnetic field range of ± 0.25 T. The red part of the curve shows the fitting of the experimental data to Eq. (7).

TABLE I: Values of fitting parameters of Hanle measurement at different temperatures (T).

T (K)	B_{SO} (T)	τ_s^* (ps)	Γ	μ (cm^2/Vs)
35	0.12 ± 0.01	88 ± 10	0.47 ± 0.05	750 ± 50
40	0.12 ± 0.01	90 ± 10	0.45 ± 0.05	580 ± 50
45	0.12 ± 0.01	67 ± 10	0.57 ± 0.05	450 ± 50
50	0.12 ± 0.01	55 ± 10	0.80 ± 0.05	400 ± 50

[1] X. Xu, W. Yao, D. Xiao, and T. F. Heinz, Nat. Phys. **10**, 343 (2014).

[2] I. Song, C. Park, and H. C. Choi, RSC Adv. **5**, 7495 (2015).

[3] Y. P. V. Subbaiah, K. J. Saji, and A. Tiwari, Adv. Funct.

Mater. **26**, 2046 (2016).
[4] A. Kuc and T. Heine, Chem. Soc. Rev. **44**, 2603 (2015).
[5] K. F. Mak, C. Lee, J. Hone, J. Shan, and T. F. Heinz, Phys. Rev. Lett. **105**, 136805 (2010).
[6] R. Das, B. Rakshit, S. Debnath, and P. Mahadevan, Phys. Rev. B **89**, 115201 (2014).
[7] H. Hatami, T. Kernreiter, and U. Zülicke, Phys. Rev. B **90**, 045412 (2014).
[8] T. Cheiwchanchamnangij, W. R. L. Lambrecht, Y. Song, and H. Dery, Phys. Rev. B **88**, 155404 (2013).
[9] H. Qiu, T. Xu, Z. Wang, W. Ren, H. Nan, Z. Ni, Q. Chen, S. Yuan, F. Miao, F. Song, G. Long, Y. Shi, L. Sun, J. Wang, and X. Wang, Nat. Commun. **4**, 2642 (2013).
[10] X. Li, F. Zhang, and Q. Niu, Phys. Rev. Lett. **110**, 066803 (2013).
[11] K. Kośmider, J. W. González, and J. Fernández-Rossier, Phys. Rev. B, **88**, 245436 (2013).
[12] A. Kormányos, V. Zólyomi, N. D. Drummond, and G. Burkard, Phys. Rev. X **4**, 011034 (2014).
[13] A. Kormányos, G. Burkard, M. Gmitra, J. Fabian, V. Zólyomi, N. D. Drummond, and V. I. Fal'ko, 2D Mater. **2**, 022001 (2015).
[14] A. Kormányos, V. Zólyomi, N. D. Drummond, P. Rakyta, G. Burkard,1 and V. I. Falko, Phys. Rev. B 88, 045416 (2013).
[15] K. F. Mak, K. L. McGill, J. Park, and P. L. McEuen, Science **344**, 1489 (2014).
[16] K. Kechedzhi and D. S. L. Abergel, Phys. Rev. B **89**, 235420 (2014).
[17] R. Suzuki, M. Sakano, Y. J. Zhang, R. Akashi, D. Morikawa, A. Harasawa, K. Yaji, K. Kuroda, K. Miyamoto, T. Okuda, K. Ishizaka1, R. Arita1, and Y. Iwasa, Nat. Nanotechnol. **9**, 611 (2014).
[18] N. Alidoust, G. Bian, S. Y. Xu, R. Sankar, M. Neupane, C. Liu, I. Belopolski, D. X. Qu, J. D. Denlinger, F. C. Chou, and M. Z. Hasan, Nat. Commun. **5**, 4673 (2014).
[19] A. V. Stier, K. M. McCreary, B. T. Jonker, J. Kono, and S. A. Crooker, Nat. Commun. **7**, 10643 (2016).
[20] Y. Song and H. Dery, Phys. Rev. Lett. **111**, 026601 (2013).
[21] D. Mastrogiuseppe, N. Sandler, and S. E. Ulloa, Phys. Rev. B **90**, 161403(R) (2014).
[22] T. Brumme, M. Calandra, and F. Mauri, Phys. Rev. B **91**, 155436 (2015).
[23] A. M. Jones, H. Yu, N. J. Ghimire, S. Wu, G. Aivazian, J. S. Ross, Bo Zhao, J. Yan, D. G. Mandrus, D. Xiao, W. Yao, and X. Xu, Nat. Nanotechnol. **8**, 634 (2013).
[24] A. M. Jones, H. Yu, J. S. Ross, P. Klement, N. J. Ghimire, J. Yan, D. G. Mandrus, W. Yao, and X. Xu, Nat. Phys. **10**, 130 (2014).
[25] Y. Ye, J. Xiao, H. Wang, Z. Ye, H. Zhu, M. Zhao, Y. Wang, J. Zhao, X. Yin, and X. Zhang, Nat. Nanotechnol. **11**, 598 (2016).
[26] L. Yang, N. A. Sinitsyn, W. Chen, J. Yuan, J. Zhang, J. Lou, and S. A. Crooker, Nat. Phys. **11**, 830 (2015).
[27] W. K. Tse, A. Saxena, D. L. Smith, and N. A. Sinitsyn, Phys. Rev. Lett. **113**, 046602 (2014).
[28] X. Lou, C. Adelmann, M. Furis, S. A. Crooker, C. J. Palmstrøm, and P. A. Crowell, Phys. Rev. Lett. **96**, 176603 (2006).
[29] X. Lou, C. Adelmann, S. A. Crooker, E. S. Garlid, J. Zhang, K. S. M. Reddy, S. D. Flexner, C. J. Palmstrøm, and P. A. Crowell, Nat. Phys. **3**, 197 (2007).
[30] N. J. Harmon, W. O. Putikka, and R. Joynt, Phys. Rev. B **79**, 115204 (2009).
[31] Y. Lu, J. Li, and I. Appelbaum, Phys. Rev. Lett. **106**, 217202 (2011).
[32] Y. Aoki, M. Kameno, Y. Ando, E. Shikoh, Y. Suzuki, T. Shinjo, M. Shiraishi, T. Sasaki, T. Oikawa, and T. Suzuki, Phys. Rev. B **86**, 081201(R) (2012).
[33] M. Drögeler, F. Volmer, M. Wolter, B. Terrés, K. Watanabe, T. Taniguchi, G. Güntherodt, C. Stampfer, and B. Beschoten, Nano Lett. **14**, 6050 (2014).
[34] O. M. J. van 't Erve, A. L. Friedman, C. H. Li, J. T. Robinson, J. Connell, L. J. Lauhon, and B. T. Jonker, Nat. Commun. **6**, 7541 (2015).
[35] M. C. Prestgard, G. Siegel, R. Roundy, M. Raikh, and A. Tiwari, J. Appl. Phys. **117**, 083905 (2015).
[36] M. Johnson and R. H. Silsbee, Phys. Rev. Lett. **55**, 1790 (1985).
[37] M. Johnson and R. H. Silsbee, Phys. Rev. B **37**, 5312 (1988).
[38] B. Huang and I. Appelbaum, Phys. Rev. B **82**, 241202(R)(2010).
[39] G. Siegel, Y. P. V. Subbaiah, M. C. Prestgard, and A. Tiwari, APL Mater. **3**, 056103 (2015).
[40] J. Jeon, S. K. Jang, S. M. Jeon, G. Yoo, Y. H. Jang, J. H. Park, and S. Lee, Nanoscale **7**, 1688 (2015).
[41] H. Schmidt, I. Yudhistira, L. Chu, A. H. Castro Neto, B. Özyilmaz, S. Adam, and G. Eda, Phys. Rev. Lett. **116**, 046803 (2016).
[42] Z. Yue, K. Tian, A. Tiwari, and M. E. Raikh, Phys. Rev. B **93**, 195301 (2016).
[43] J. Yan,J. Xia, X. Wang, L. Liu, J. L. Kuo,B. K. Tay, S. Chen, W. Zhou, Z. Liu, and Z. X. Shen, Nano lett. **15**, 8115 (2015).
[44] A. Allain, J. Kang, K. Banerjee, and A. Kis, Nat. Mater. **14**, 1195 (2015).
[45] W. Wang, Y. Liu, L. Tang, Y. Jin, T. Zhao, and F. Xiu, Sci. Rep. **4**, 6928 (2014).
[46] F. J. Jedema, H. B. Heersche, A. T. Filip, J. J. A. Baselmans, and B. J. van Wees, Nature (London) **416**, 713 (2002).
[47] R. C. Roundy, M. C. Prestgard, A. Tiwari, and M. E. Raikh, Phys. Rev. B **90**, 205203 (2014).
[48] R. C. Roundy, M. C. Prestgard, A. Tiwari, E. G. Mishchenko, and M. E. Raikh, Phys. Rev. B **90**, 115206 (2014).
[49] P. Li and I. Appelbaum, Phys. Rev. B **92**, 195129 (2015).
[50] We define $R_0 = P^2\rho d/(8\sqrt{\pi}A)$. For our trilayer MoS_2 system, we calculated R_0 is about 350 $\Omega \cdot m/s$ assuming P is 0.7.
[51] P. Li, J. Li, L. Qing, H. Dery, and I. Appelbaum, Phys. Rev. Lett. **111**, 257204 (2013).